AIAA JOURNAL
Vol. 37, No. 10, October 1999

Numerical Investigation of Supersonic Injection Using a Reynolds-Stress Turbulence Model

Clarence F. Chenault* and Philip S. Beran†
Air Force Institute of Technology, Wright–Patterson Air Force Base, Ohio 45433-7542
and
Rodney D. W. Bowersox‡
University of Alabama, Tuscaloosa, Alabama 35487

The full, three-dimensional Favré-averaged Navier–Stokes equations, coupled with the second-order Zhang et al. (Zhang, H., So, R., Gatski, T., and Speziale, C., "A Near-Wall Second-Order Closure for Compressible Turbulent Flows," *Near-Wall Turbulent Flows*, edited by R. So, C. Speziale, and B. Launder, Elsevier, New York, 1993, pp. 209–218) Reynolds-stress turbulence and K–ϵ models, were used to numerically simulate a 25-deg, Mach 1.8 injection into a Mach 3.0 crossflow. Detailed comparisons with experimental data were performed. Analysis of the Reynolds-stress turbulence model simulation results revealed physically consistent and accurate predictions for mean flow and turbulent quantities, whereas the simulations with the K–ϵ model resulted in nonphysical and inconsistent turbulence predictions. Analysis of the three-dimensional flowfield simulation with the Reynolds-stress turbulence model shows that the shock structure downstream of the oblique barrel shock was a mirrored image of the leeward side of the oblique barrel shock. Furthermore, the downstream location where vortical motion was initiated in the jet plume was caused by the recompression shock-induced vortices. These vortices were generated through the combined effects of the inflow air upwash behind the plume and the mirrored oblique barrel shock.

Nomenclature

D^t, D^v = turbulent and viscous diffusion
D_ϵ, D^t_ϵ = dissipation-rate destruction and diffusion
D^v_ϵ = viscous diffusion of dissipation rate
d = exit diameter of nozzle
E = specific total energy
e = specific internal energy
f_μ = turbulence model wall damping functions
H = specific total enthalpy
i, j, k = grid dimension
K = turbulence kinetic energy
M = Mach number
M_{ij} = mass flux variation
n = normal to surface
P_{ij}, P_ϵ = turbulent and dissipation production
p = static pressure
q_i = heat-transfer rate per unit area
T = temperature
t = time
$\boldsymbol{u}_i$ = velocity vector
$\boldsymbol{x}_i$ = position vector
γ = ratio of specific heats
δ_{ij} = Kronecker delta
ϵ = turbulence dissipation rate
ϵ_{ij} = turbulence dissipation-rate tensor components
κ = thermal conductivity coefficient
λ = second bulk viscosity coefficient
μ = first bulk viscosity coefficient molecular viscosity
μ_t = turbulent eddy viscosity
Π_{ij} = pressure dilatation
ρ = density
σ_{ij} = shear-stress tensor components
τ_{ij} = Favré-averaged Reynolds-stress tensor components

Subscripts

j = jet quantity
t = stagnation value, turbulent value
wall = wall value
∞ = freestream or undisturbed value

Superscripts

$\tilde{}$ = mean value of Favré-averaged variable
$''$ = fluctuating value of Favré-averaged variable
$\bar{}$ = time-averaged value

Introduction

RESURGENT interest in supersonic/hypersonic vehicles and highly maneuverable aircraft employing thrust-vector control has prompted a flurry of experimental and numerical investigations attempting to describe the flowfield generated by transverse jet injection into supersonic flow (TJISF).[1–8] Comprehensive descriptions and accurate predictions of the shock structure and turbulence generated by this flowfield are critical to the design of scramjet combustors,[9] film-cooled turbine fans,[10] rocket-motor thrust-vector regulation systems[11] and high-speed vehicles using reaction control jets.[11] However, incomplete data describing the physics of the flowfield and the accompanying turbulent stresses generated by TJISF continue to hinder major advances in many areas of the aerospace industry.

One of the driving thrusts of research into TJISF is enhanced mixing of fuel and air in SCRAMjet combustors. Thrust production from a SCRAMjet is often described as mixing limited[9] because the time available to mix the fuel and air, combust the mixture, and exhaust the products is on the order of milliseconds.[3,4] Among other things, mixing efficiency is dependent on injection angle, fuel-to-air pressure ratio, total pressure and shock losses, and fuel penetration depth.[9]

Presented as Paper 98-3425 at the AIAA/ASME/SAE/ASEE Joint Propulsion Conference, Cleveland, OH, 13–15 July 1998; received 23 October 1998; revision received 23 February 1999; accepted for publication 26 February 1999.

*Graduate Research Assistant; currently Airframe Integration Engineer and CFD Analyst, U.S. Air Force Research Laboratory, Air Vehicles Directorate, Aeronautical Sciences Division; clarence.chenault@va.wpafb.af.mil. Senior Member AIAA.

†Adjunct Associate Professor, Department of Aeronautics and Astronautics, and Senior Research Aerospace Engineer, U.S. Air Force Research Laboratory. Senior Member AIAA.

‡Assistant Professor, Department of Aerospace Engineering and Mechanics. Senior Member AIAA.

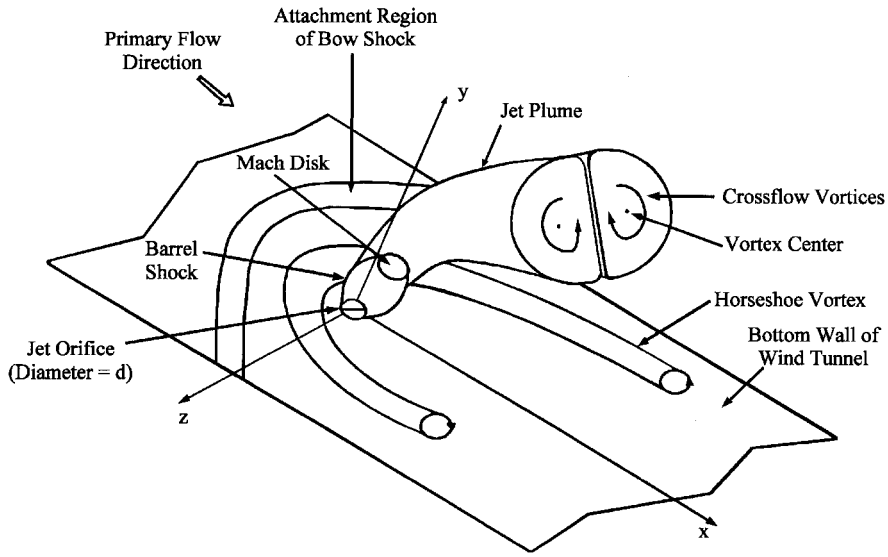

Fig. 1 Schematic of a three-dimensional normal injection flowfield.[6]

Injection angle is critical to fuel penetration depth, and a compromise between the two extremes of normal and tangential injection is oblique injection. Mays et al.[4] has shown that oblique injection can result in deep injectant penetration and still have a significant contribution to the streamwise momentum of the exhaust. Thus, the potential advantages of oblique injection have resulted in many studies trying to characterize this injection technique.[1–8,12]

A discussion by Santiago and Dutton[6] of the three-dimensional flowfield shown in Fig. 1 reveals the limited knowledge currently available for this class of flowfields. Depicted in Fig. 1 is the flowfield generated by TJISF through a circular nozzle normal to the freestream. It is generally accepted that a bow shock is generated in the freestream by the obstruction of the injectant (not shown) and that after leaving the orifice the jet expands through a Prandtl–Meyer fan, recompresses through a barrel shock, and ends with a sonic disk (Mach disk). Within the plume the injectant is turned downstream and at some point within the jet plume, a pair of counter-rotating crossflow vortices form. Santiago and Dutton[6] assert that this vortical or secondary flow is the primary source of entrainment of the surrounding inflow air into the injectant. Other vortical structures identified by Santiago and Dutton[6] are the horseshoe vortices (a secondary flow), which wrap around the upstream side of the jet and trail downstream, and wake vortices periodically shed near the base of the inner jet core.

Missing from Santiago and Dutton's discussion of the flowfield is an analysis detailing where the crossflow vortices form within the plume, the mechanisms that start the rotation, and a description of the flowfield immediately surrounding the nozzle orifice. This omission is typical of the discussions for similar flowfields investigated.[2–5,8,13–17]

Accurate predictions of the turbulent Reynolds stresses are critical to a better understanding of how the mean flow variables interact with the turbulent eddies created by injection,[4,6] and the high cost associated with full-scale wind-tunnel testing dictates that potential engine designs be dry tested prior to wind-tunnel testing and test stand firing. One of the most cost-effective methods for dry testing a design is computational fluid dynamics (CFD). Unfortunately, the full potential of CFD for the study of TJISF is still far from being realized because of a lack of robust turbulence models capable of accurately describing the complex turbulent flowfield generated by TJISF.

Efforts to numerically simulate three-dimensional injection flowfields have historically been confined to algebraic mixing-length models and eddy viscosity models.[8,12,17–19] Although these simulations have provided the engineering community with gross estimates of the flowfield structure, these classes of turbulence models are incapable of correctly modeling secondary flow structures or turbulent stresses associated with injection flowfields.[20,21] The overriding deficiency of these model formulations is their inability to correctly model the components of the Reynolds-stress tensor τ_{ij} (Ref. 21). This tensor, henceforth referred to as the Favré-averaged Reynolds-stress tensor (FARST), represents the fluctuating stresses encountered in a turbulent flowfield and is defined in component form as

$$\tau_{ij} \equiv \overline{u_i'' u_j''} \tag{1}$$

where the double-primed velocities represent the Favré-averaged fluctuating component of the instantaneous velocities and the overbar represents time averaging.

In eddy viscosity models the FARST is modeled with the Boussinesq approximation, which states "that the principal axes of the ... [components of the FARST] ... are coincident with those of the mean strain-rate tensor, S_{ij}, at all points in a turbulent flow, ... [where] ... the constant of proportionality between τ_{ij} and S_{ij} is the eddy viscosity, μ_t."[21] This approximation provides adequate results for a limited number of flowfields but often provides poor turbulent stress predictions for many other flowfields, including three-dimensional flows, flows in ducts with secondary motions, and rotating flows.[21]

Second-order Reynolds-stress models (RSTM) can predict secondary flow structures and the Reynolds stresses found in the aforementioned flowfields, but these models are much more complex than the eddy viscosity models. In addition to the five thermomechanical equations, RSTMs require six transport equations to describe the behavior of τ_{ij} and a seventh equation to model the transport of the dissipation rate. An RSTM overcomes many shortcomings inherent to the Boussinesq approximation because it automatically accounts for convection and diffusion of τ_{ij} and the effects of flow history.[21] These models also include convection and production terms that automatically respond to effects such as streamline curvature and system rotation.[21] Finally, the RSTM "gives no a priori reason for the normal stresses to be equal when the mean strain rate vanishes. Rather their values will depend upon initial conditions and other flow processes, so that the model should behave properly for flows with sudden changes in strain rate."[21]

This paper builds on the numerical investigation results presented in Chenault et al.[22] This investigation takes advantage of recent advances in computational resources to numerically simulate the three-dimensional injection experiments of McCann and Bowersox.[5] Using the second-order Zhang, So, Gatski, and Speziale (ZSGS) RSTM[23] to provide turbulence closure, this investigation validates the ZSGS RSTM for TJISF and presents a detailed analysis of the turbulent flowfield surrounding the nozzle orifice. This analysis identifies the region where rotation starts within the jet plume and the mechanism that causes the rotation.

A detailed description of the experimental configuration numerically simulated for this study is found in Ref. 5. However,

Table 1 Injection parameters[5]

Parameter	Value
P_{t_j}/P_{t_∞}	1.93
P_j/P_∞	10.5
u_j/u_∞	0.79
ρ_j/ρ_∞	6.47
$(\rho u)_j/(\rho u)_\infty$	5.12

Table 2 Normalized random error analysis results[24]

Measurement	Error, %
p_t/p_{t_∞}	11.0
$\overline{\rho u_i}/(\rho u)_\infty$	6.0
Reynolds stresses	20.0

the features salient to this simulation are outlined next. Freestream conditions at the wind-tunnel test section entrance were $M_\infty = 2.9$, $Re/m = 15 \times 10^6$, $P_{t_\infty} = 2.0 \pm 0.03$ atm, and $T_{t_\infty} = 294 \pm 2$ K. The wind tunnel's rectangular test section was 28 cm long with cross-sectional dimensions of 6.35×6.35 cm. A conical nozzle was used to inject pressurized air at a Mach number of 1.8 into the inflow air. The injector was set along the centerline of the test section floor and angled 25 deg downstream. The nozzle throat and exit diameters were 3.264 and 3.861 mm, respectively. Because the injector was at an angle, the exit port was elliptical with major and minor axes measuring 9.14 and 3.861 mm. The exit diameter of the conical nozzle $d = 3.861$ mm is used as the reference length throughout this study. The injectant total pressure and temperature were 3.8 ± 0.03 atm and 294 ± 2 K. Table 1 summarizes the injection mean flow parameters.

McCann and Bowersox reported mean flow and turbulence data 20 diameters downstream of the nozzle exit, and to facilitate comparison of the numerical results to the experimental data their data collection grid is superimposed over the contour plots of variables for which experimental data are available. Numerical uncertainty estimates provided by McCann and Bowersox are summarized in Table 2 (Ref. 24).

Numerical Solver and Governing Equations

The numerical solver used for this study was NASA Langley Research Center's ISAAC.[25] ISAAC was selected for this study because it is a reasonably mature program with documented validation of the turbulence models incorporated into its solution algorithm.[25,26]

ISAAC is a three-dimensional finite volume program that uses time integration of the governing equations. The integration is performed with a diagonalized, approximate factorization scheme.[25] Second-order spatial accuracy for the inviscid terms is attained with the MUSCL scheme of van Leer[27] and a generalized form of Roe's approximate Riemann solver,[28] and the Venkatakrishnan limiter[29] is used to avoid spurious oscillations in the neighborhood of discontinuities.

The governing equations for this flowfield are the Favré-averaged Navier–Stokes (FANS) equations coupled with either the second-order ZSGS RSTM[23] or the ZSGS K–ϵ model.[23] The forms of the FANS equations incorporated by Morrison[25] into ISAAC:

$$\bar{\rho}_{,t} + (\bar{\rho}\tilde{u}_k)_{,k} = 0 \tag{2}$$

$$(\bar{\rho}\tilde{u}_i)_{,t} + (\bar{\rho}\tilde{u}_i\tilde{u}_k + \bar{p}\delta_{ik})_{,k} - (\tilde{\sigma}_{ik} - \bar{\rho}\tau_{ik})_{,k} = 0 \tag{3}$$

$$(\bar{\rho}\tilde{E})_{,t} + (\bar{\rho}\tilde{u}_k\tilde{H})_{,k} - \left(D^v_{ii} + D^t_{iik} + \tilde{u}_i\tilde{\sigma}_{ik}\right)_{,k}$$
$$- (\overline{u''_i\tilde{\sigma}_{ik}} - \bar{\rho}\tilde{u}_i\tau_{ik} - \tilde{q}_k - C_p\bar{\rho}\overline{u''_kT''})_{,k} = 0 \tag{4}$$

where $(\cdot)_{,*}$ indicates a partial derivative with respect to time or the spatial coordinate x_i. The nomenclature used in these equations is defined as $\tilde{E} \equiv \tilde{e} + \frac{1}{2}\tilde{u}_i\tilde{u}_i + K$, specific total energy; $\tilde{H} \equiv \tilde{h} + \frac{1}{2}\tilde{u}_i\tilde{u}_i + K$, specific total enthalpy; $\tilde{\sigma}_{ik} = 2\bar{\mu}\tilde{S}_{ik} + \lambda\tilde{S}_{jj}\delta_{ik}$, components of the shear-stress tensor, where Stokes hypothesis $\lambda = -\frac{2}{3}\mu$; $\tilde{S}_{ik} = \frac{1}{2}(\tilde{u}_{i,k} + \tilde{u}_{k,i})$, components of the strain-rate tensor; $\tilde{q}_k = -\kappa\tilde{T}_{,k}$, convective heat flux; $D^v_{ii} = \overline{u'_i\sigma'_{ik}}$, viscous diffusion of turbulent stresses; $D^t_{iik} = -\frac{1}{2}\bar{\rho}\overline{u''_ku''_iu''_i}$, turbulent diffusion of turbulent stresses; $C_p\bar{\rho}\overline{u''_kT''}$, turbulent heat flux; $K = \tau_{ii}/2$, turbulent kinetic energy; and $\tau_{ik} = \overline{u''_iu''_k}$, FARST. This definition of τ_{ik} is adopted to maintain consistency with sources and software cited from the NASA Langley Research Center; the more common definition is $\tau_{ik} = -\rho\overline{u''_iu''_k}$.

In this study, turbulence closure of Eqs. (2–4) is achieved with either the ZSGS RSTM or the ZSGS K–ϵ model. Although several other Reynolds stress and K–ϵ turbulence models are available in ISAAC, these two were selected because they were specifically developed for supersonic compressible flows, and both have been extensively validated for flat plate flowfields,[23] flowfields generated by compression ramps,[26] and flows around axisymmetric bodies.[25] The desirability of these two models for this study was further enhanced by the fact that the ZSGS K–ϵ model is a contracted form of the ZSGS RSTM, thus allowing a direct comparison of the results without excessive qualification of the development of the two models.

The conservative forms of the Favré-averaged, Reynolds-stress transport equation as incorporated in ISAAC is[25]

$$(\bar{\rho}\tau_{ij})_{,t} + (\bar{\rho}\tilde{u}_i\tau_{ij})_{,k} = D^v_{ijk,k} + D^t_{ij,k} + P_{ij} - \bar{\rho}\epsilon_{ij} + \Pi_{ij} + M_{ij} \tag{5}$$

Contracting Eq. (5) results in the K transport equation, which is given as

$$(\bar{\rho}K)_{,t} + (\bar{\rho}\tilde{u}_{,k}K)_{,k} = D^v_{iik,k} + D^t_{ii,k} + P_{ii} - \bar{\rho}\epsilon_{ii} + \Pi_{ii} + M_{ii} \tag{6}$$

Both models share a common form of the dissipation-rate ϵ transport equation, which is given as

$$(\bar{\rho}\epsilon)_{,t} + (\bar{\rho}\tilde{u}_k\epsilon)_{,k} = D^v_{\epsilon,k} + D^t_{\epsilon,k} + P_\epsilon - D_\epsilon + \Psi + \xi \tag{7}$$

The Boussinesq approximation used to compute the Reynolds stresses in the K–ϵ model is formulated as

$$\tau_{ij} = -2(\mu_t/\bar{\rho})\left(\tilde{S}_{ij} - \tfrac{1}{3}\tilde{S}_{kk}\delta_{ij}\right) + \tfrac{2}{3}K\delta_{ij} \tag{8}$$

where

$$\mu_t = C_\mu f_\mu \bar{\rho}(K^2/\epsilon) \tag{9}$$

Closure constants and models for the many higher-order terms in Eqs. (2–9) are provided by Zhang et al.[23] and Chenault.[30]

In addition to the turbulence models, an equation of state must be specified for system closure. The perfect gas equation of state used for this study is

$$\bar{p} = \bar{\rho}(\gamma - 1)\left(\tilde{E} - \tilde{u}_i^2/2 - K\right) \tag{10}$$

where γ is the ratio of specific heats.[31]

Boundary and Initial Conditions

The computational domain for the grid used in this study had six sides. In this grid the plane defined by $y/d = 0$ corresponds to the solid surface of the test section with a hole cut in it for the jet, whereas the planes at the streamwise extremes are the inflow and outflow planes.

Because the undisturbed freestream in the test section is supersonic, all dependent variables were assigned their respective freestream values as an initial condition. (An inflow boundary layer was not modeled.) For this purpose a turbulence intensity (TI) is defined as $\mathrm{TI} \equiv \sqrt{(2/3K_\infty)}/u_\infty$, where the value of TI was taken as 0.016% (Ref. 5). Thus, for the K–ϵ model, K_∞ is computed directly from the definition of TI such that $K_\infty = \frac{3}{2}(\mathrm{TI}u_\infty)^2$. For the RSTM the initial values of τ_{xx}, τ_{yy}, and τ_{zz} are determined by assuming the freestream turbulence is homogeneous and isotropic. Thus, from the definition $K \equiv (\tau_{xx} + \tau_{yy} + \tau_{zz})/2$ one arrives at $\tau_{xx_\infty} = \tau_{yy_\infty} = \tau_{zz_\infty} = 2/3K_\infty$ and $\tau_{xy_\infty} = \tau_{xz_\infty} = \tau_{yz_\infty} = 0$.

The freestream dissipation rate for both turbulence models is commonly found by setting $\mu_{t_\infty} = \mu_\infty$ in Eq. (9) such that $\epsilon_\infty = \rho_\infty K_\infty^2/\mu_\infty$ (Refs. 11 and 18).

At the test-section surface, the no-slip condition $u = v = w = 0$ is invoked along with $\partial p/\partial n = 0$ and the adiabatic wall condition $\partial T/\partial n = 0$. The homogeneous condition applies to the Reynolds stresses at the wall such that $K = \tau_{ij} = 0$. To maintain asymptotic consistency at the wall, $\epsilon = 2\bar{\nu}(\partial\sqrt{K}/\partial y)^2$ is used as the boundary condition for the dissipation-rate equation.[25]

Injectant mean flow properties used for this simulation are listed in Table 1 and correspond to fluid injection at Mach 1.8. However, at the interface between the lower test section wall and the nozzle exit a discontinuity exists. During the initial phase of this research, this discontinuity resulted in unstable behavior in the solution algorithm. Therefore, a blending algorithm simulating a boundary layer at the edge of the nozzle is used to smooth transition between the surrounding flowfield properties and injectant mean flow properties. This boundary layer is simulated with a truncated and shifted tanh function. The details of its implementation are found in Ref. 30.

Ideally, turbulence levels for K, τ_{ij}, and ϵ should be specified along injector exit boundary. However, this information is generally not available for computational efforts. Therefore, in a manner similar to that used by Rizzetta,[11] uniform boundary conditions of $\partial K/\partial n = \partial\tau_{ij}/\partial n = \partial\epsilon/\partial n = 0$ are used for the turbulence variables at all locations over the outflow plane of the nozzle. The acceptability of the numerical results based on these conditions must be evaluated by comparison of the numerical results with the experimental data.

At the streamwise outflow plane the x–y planes at the sides of the domain and the upper x–z plane, a first-order extrapolation from the interior was used as the boundary condition such that $\partial(*)/\partial n = 0$, where $*$ is any of the conserved variables and n is the coordinate normal to the surface of interest.

Results

Quantitative and qualitative comparisons and evaluations of numerical simulation results and experimental data are reported in this section. This section begins with a discussion of the grid-resolution study performed to arrive at the grid configuration used in this study. This is followed by a quantitative evaluation of selected mean flow and turbulent quantities simulated with the two turbulence models and a comparison of these simulations to experimental data. This section concludes with a qualitative evaluation of the flowfield expansion/shock structure simulated with the ZSGS RSTM and a discussion of the flowfield mechanisms that generate the vortical motion within the injection plume.

Computational Grid

The computational grid used in this study (Fig. 2) has i, j, k dimensions of $275 \times 106 \times 102$ and physical dimensions of $x/d = -5$–21, $y/d = 0$–5.2, and $z/d = -3.25$–3.25. Spatial modeling of the nozzle outflow plane consisted of 92 equidistantly spaced streamwise nodes and 43 equidistantly spaced spanwise nodes. Spatial modeling of the flowfield upstream of the nozzle consisted of 49 streamwise nodes, and the remaining 135 streamwise nodes were used to model the flow downstream of the nozzle. One-dimensional tanh stretching was used in all regions that were not equidistantly spaced. In the normal direction, away from the solid wall, an initial spacing ensuring $y^+ < 1$ was used. The domain of this grid was not required to extend to the upper and side walls of the test section because the reflected shocks from these walls did not interact with the injection flowfield prior to $x/d = 20$ (station 20).

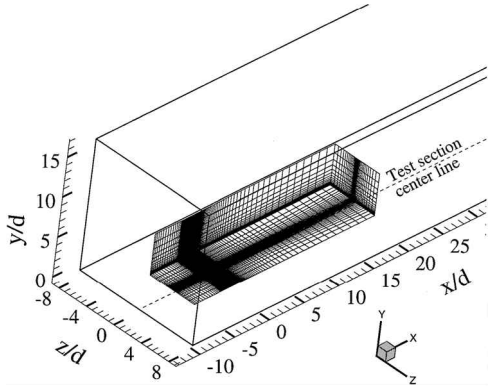

Fig. 2 Computational grid.

The mesh sensitivity studies conducted to arrive at this grid configuration consisted of examination of coarse, medium, and fine grid meshes. Each of the conserved variables was examined for spatial convergence in the x–y plane defined by $z/d = 0$ and the y–z plane defined by $x/d = 8.0$. Streamwise and normal grid-convergence sensitivity studies were conducted using grids with $i \times j$ dimensions of 181×61, 339×121, and 508×181, respectively. These grids were evaluated for spatial convergence of all conversed variables. The contour plots shown in Fig. 3 for the U component of velocity are characteristic of all of the conserved variables. In these contour plots there are clear differences between the results of the coarse and the medium grids, and although there were some differences between the results of the medium and the fine grids, they were significantly smaller than the results of the previous comparison. Grid convergence in the x–y plane had been obtained with the two finest grids, and in light of the limited resources available for the full three-dimensional simulations, the dimensions and spacing of the medium grid were used for the x–y plane.

Transverse grid-convergence sensitivity studies were also conducted for the conserved variables. This study was performed using grids with $i \times j \times k$ dimensions of $261 \times 121 \times 31$, $261 \times 121 \times 61$, and $261 \times 121 \times 91$, respectively, for the coarse, medium, and fine grids. Each of these grids modeled half of the test section, and the streamwise domain was limited to $x/d = 8.0$ to reduce the computational resources and run times required to preform the simulations. The streamwise spacing up to $x/d = 8.0$ used the spacing, which was determined to be grid convergent in the preceding section. This location ($x/d = 8.0$) was selected as the streamwise limit because experimental data and the two-dimensional simulation results implied that the structure of the flowfield did not undergo drastic changes beyond this point. Thus, the assumption was made that if the solution was grid converged in the y–z plane at this streamwise location extensions of the grid to other downstream locations would also be grid converged in the y–z plane.

The contour plots shown in Fig. 4 for the V component of velocity are characteristic of all of the conserved variables. As with the two-dimensional analysis in the x–y plane, there were clear differences between the results of the coarse and medium grids for each of the variables examined. And again, although there were some differences between the results of the medium and fine grids, they were significantly smaller than the differences seen in the preceding comparison. Thus, grid convergence in the y–z plane had been obtained with the two finest grids, and once again, in light of the limited resources available for the full three-dimensional simulations and the run-time requirements of the RSTM, the dimensions and spacing of the medium grid were used for the y–z plane.

Two techniques were used to determine convergence of the calculations. Initially, the L2 norm of the residual was followed as an indicator of error reduction. Once the residual values had leveled off or began oscillating about some fixed value (usually after decreasing three orders of magnitude), the solution itself was monitored. Convergence was declared once the general flow properties such as Mach number, static pressure, and K had stopped changing when visually inspected on contour plots.

Comparison to Experimental Data

Two distinct flow regions are identified in the contour plots of the experimental data collected at station 20 for the mean flow and turbulence variables. In the middle part of each contour plot is the injectant plume, and in the lower part of the plot is the boundary layer. The separation of the plume and boundary layer is clearly seen in the experimental data for the U component of velocity (Fig. 5a). In this figure there is a region where the streamwise velocity of the plume is markedly different from the surrounding flowfield. At this station the axial velocity in the plume has increased from the initial nondimensional streamwise velocity ($U = \tilde{u}/\tilde{a}_\infty$) of 2.2 at the nozzle exit to about 2.6. This is still lower than the surrounding flowfield's streamwise velocity of 2.8. The lateral extent of the jet

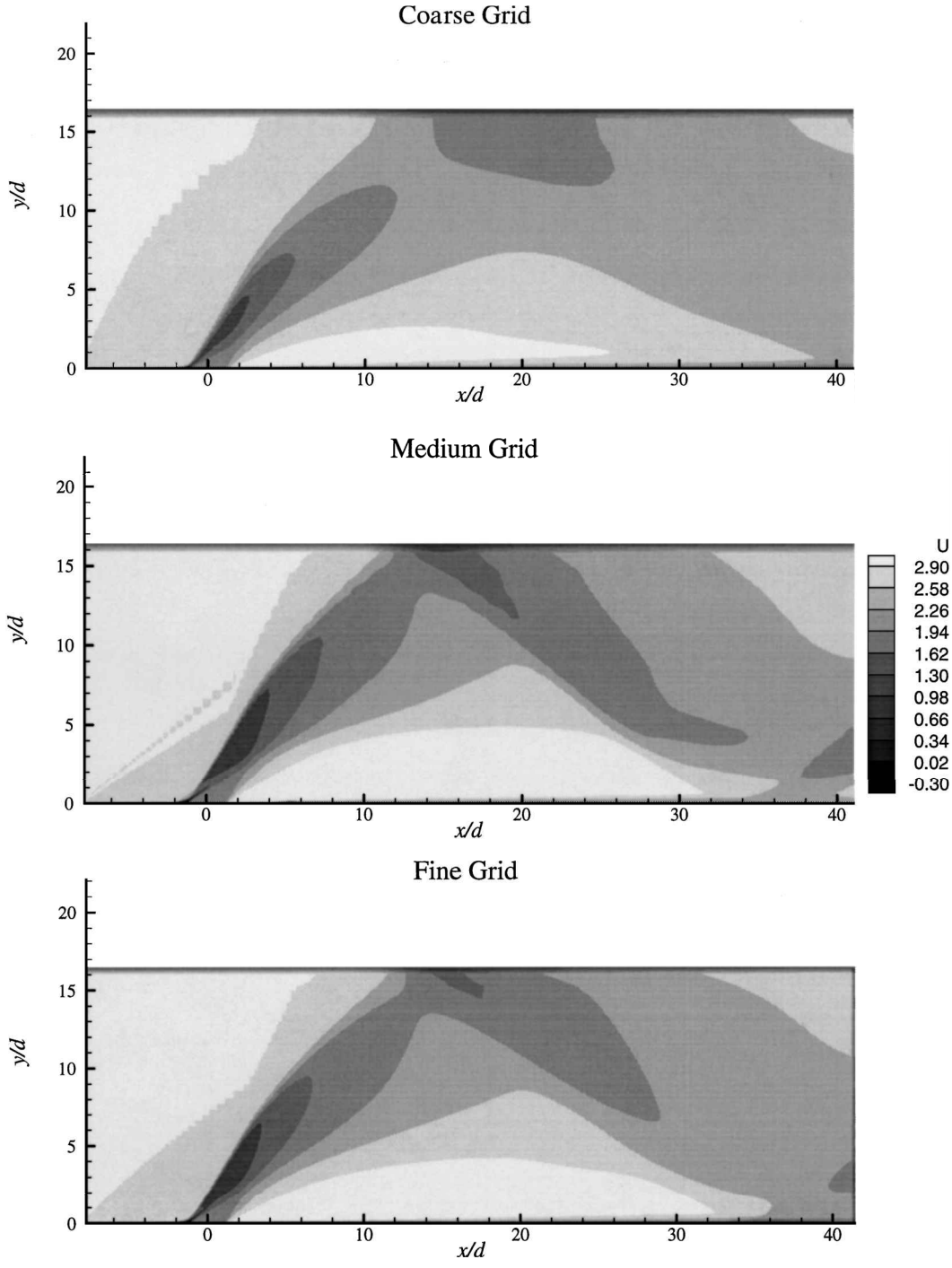

Fig. 3 Two-dimensional mesh study results for U component of velocity.

plume has increased from the initial value of $1.036d$ at the nozzle exit to approximately $3.75d$. A bottleneck in the contours form on the lower side of the plume as the injectant rises farther above the boundary layer with increasing distance downstream of the nozzle. The indentations along the bottom of the plot at $z/d = 0.0$ and 2.0 indicate the upper limits of the boundary layer.

Only minor differences are seen in the predictions from the two turbulence models for the U component of velocity (Figs. 5b and 5c). In these figures the height, vertical extent, and lateral extent are measured as shown in Fig. 5b. These figures show the predictions from both models agree well with the experimental data. The predicted height from the RSTM of $4.0d$ (Fig. 5c) is only 1% less than the experimentally measured value of $4.03d$, and the height from the K–ϵ model of $4.2d$ (Fig. 5b) is only 4% greater than the experimental value. The numerical predictions for the vertical extent of the plume are $2.6d$ from RSTM and $2.7d$ from K–ϵ. Both of these predictions are in good agreement with the experimentally measured value of $2.62d$ (1.5% for RSTM and 3% for K–ϵ). The numerical predictions for the lateral extent of the plume have poorer agreement with the experimentally measured value of $3.7d$. Both models predicted lateral extents of $2.90d$, or a 21% difference. Although the numerical results for the lateral extent are disappointing, they are consistent with numerical results reported by Fuller and Walters.[13] Generally, the predicted magnitude from both models of U surrounding the plume is slightly larger than the experimentally measured magnitudes over most of the domain. This may be a consequence of assuming uniform inflow conditions rather than simulating an inflow boundary layer.

Some minor asymmetric behavior about $z/d = 0.0$ that does not appear in the numerical results is seen in the experimental data. Asymmetries such as these are also reported by Hartfield and Bayley,[14] Wilson et al.,[32] and Mays et al.[4] This asymmetric

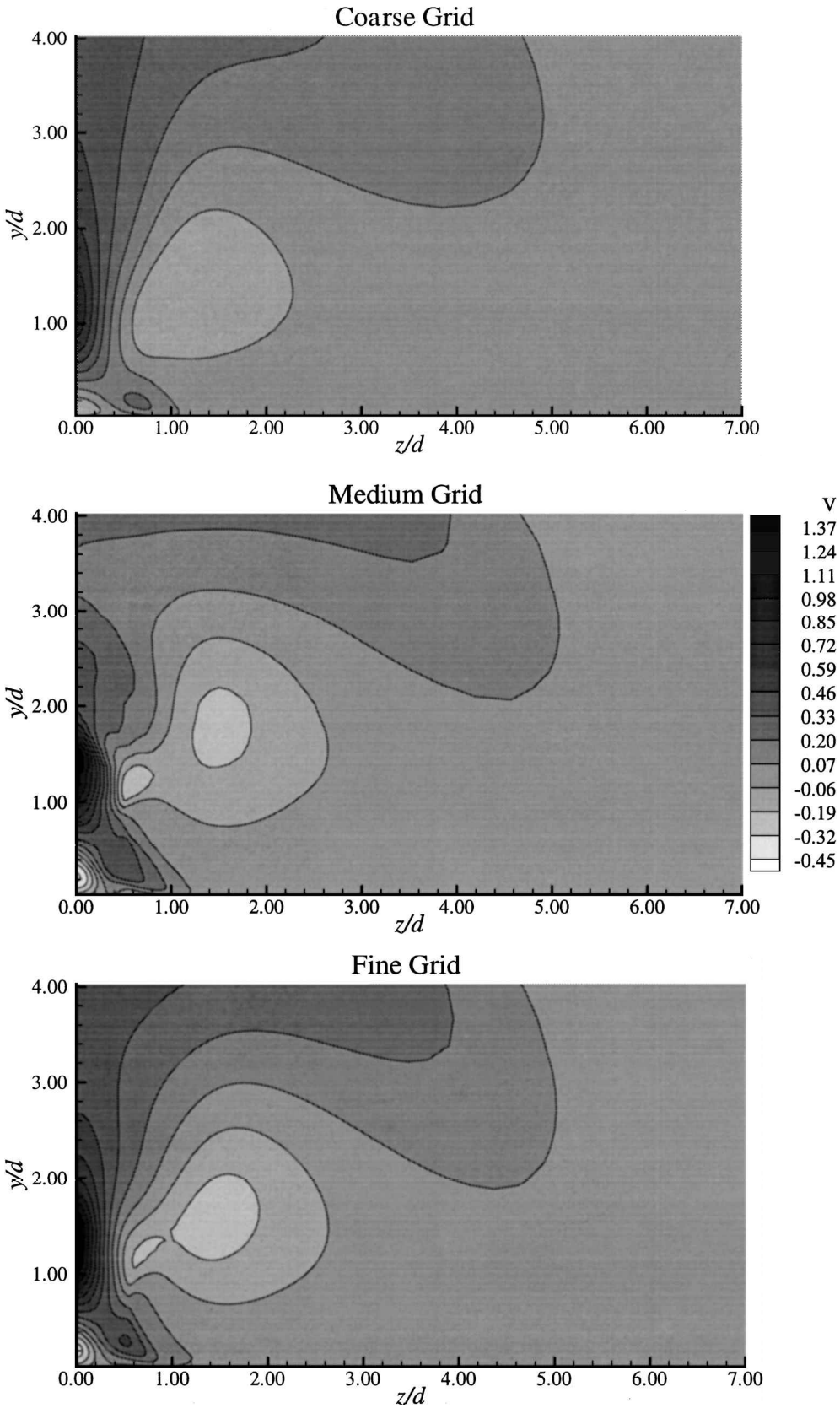

Fig. 4 Three-dimensional mesh study results for V component of velocity.

behavior may be attributable to a combination of imperfections in the test section and nozzle, systematic errors in the data collection procedure, and the coarseness of the data collection matrix.[5,30] It is equally possible these asymmetries are caused by unstable transients in the flowfield, which are damped out of the numerical solution.

The experimental data seen in Fig. 6a for τ_{xy}, where $\tau_{xy}/U^2 = (\tau_{xy_d}/a_\infty^2)(a_\infty^2/\tilde{u}^2) = \tau_{xy_d}/\tilde{u}^2$ and both τ_{xy_d} and $\tilde{u}$ are dimensional quantities, show a central core of positive shear stress slightly offset to the right of the centerline. However, the extent of positive shear stress is relatively symmetric about the centerline. This positive shear stress is surrounded by a horseshoe-shaped region of negative shear stress, which is also centered about the line defined by $z/d = 0.0$. However, the magnitude of the negative shear stress is greater on the side where $z/d < 0.0$.

The predicted structure of τ_{xy} is not consistent between the two turbulence models. The horseshoe-shaped region and the positive

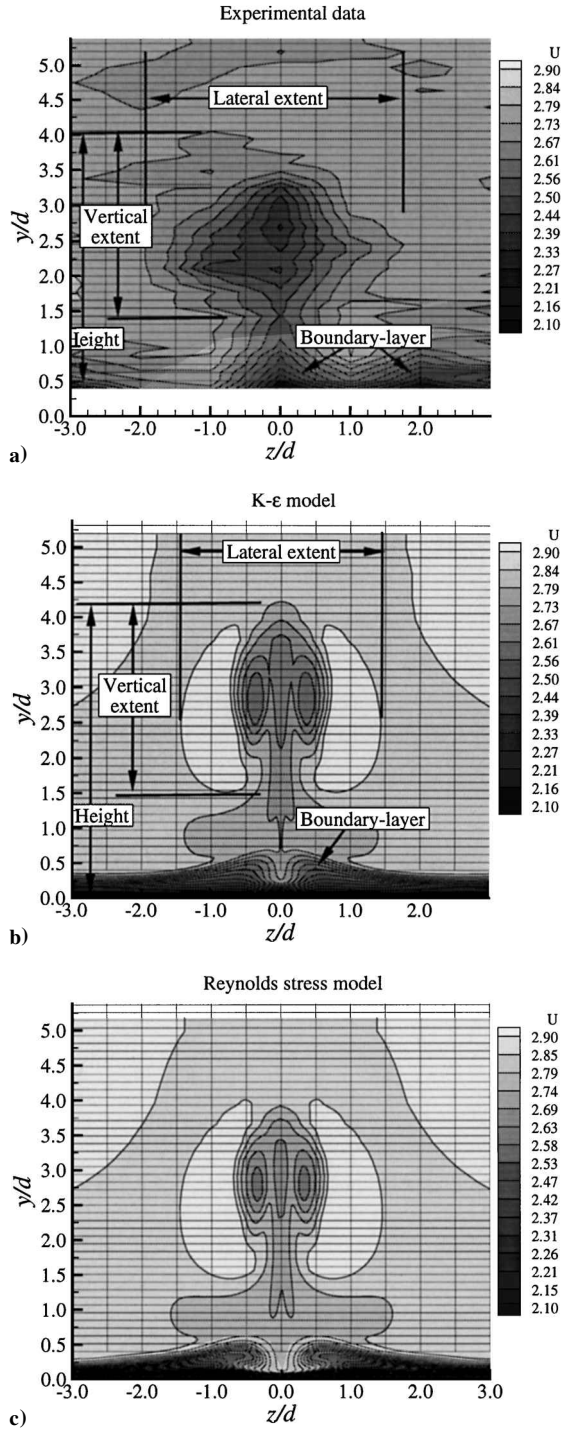

Fig. 5 *U* **component of velocity at station 20 with experimental data collection grid overlaid ($U = \tilde{u}/\tilde{a}_\infty$).**

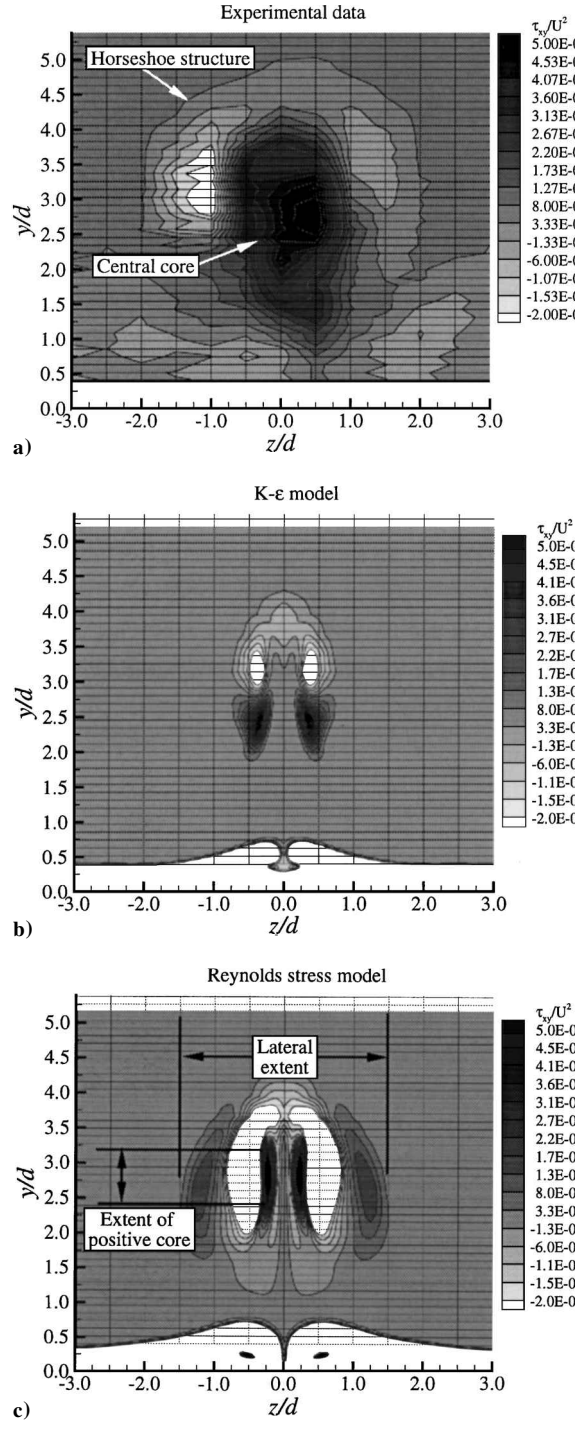

Fig. 6 τ_{xy} **at station 20 with experimental data collection grid overlaid.**

central core identified in Fig. 6a are predicted by both turbulence models. However, as seen in Figs. 6b and 6c, only the RSTM correctly predicted the relative location of the horseshoe structure with respect to the central core. The K–ϵ model incorrectly predicted the location of the horseshoe structure, placing it well above the central core of positive stress.

In general, the RSTM predictions for τ_{xy} are consistent with the experimental data in that they smoothly progress from the large positive values in the central core to the negative values away from the centerline. In contrast to this, the K–ϵ predictions simply reflect a change in the sign of $\partial U/\partial y$.

A mathematical explanation of the differences is readily available if a Cartesian coordinate system centered at $z/d = 0.0$ and $y/d = 2.75$ is superimposed over the contours in Fig. 6. In the K–ϵ model τ_{xy} is computed from Eq. (8) and is of the form

$$\tau_{xy} = -\frac{\mu_t}{\bar{\rho}}\left(\frac{\partial U}{\partial y} + \frac{\partial V}{\partial x}\right) \tag{11}$$

At station 20, $\partial V/\partial x \ll \partial U/\partial y$, and from the results shown in Figs. 6b and 6c, within the plume $\partial U/\partial y$ dominates $\partial V/\partial x$. Thus, in the two upper Cartesian quadrants τ_{xy} is negative because $\partial U/\partial y$ is positive, and in the two lower Cartesian quadrants τ_{xy} is positive because $\partial U/\partial y$ is negative. Furthermore, because $\partial U/\partial z$ is not accounted for in Eq. (11), the K–ϵ model predictions for τ_{xy} near the edges of the plume are negligible.

In contrast to the K–ϵ model, predicted changes in τ_{xy} from the RSTM correspond to radial changes in the velocity gradients. When a radial line drawn from the origin of the superimposed Cartesian coordinate system passes through negative gradients of U, τ_{xy} becomes more positive, and when positive gradients are encountered, τ_{xy} becomes more negative.

In addition to correct qualitative predictions for τ_{xy} from the RSTM, its quantitative predictions also show good agreement with the experimental data. The RSTM correctly predicted the range of the vertical extent of the positive shear stress, placing it between $y/d = 2.4$ and 3.3, whereas the K–ϵ model incorrectly places the range between $y/d = 2.3$ and 2.7. The experimentally determined range is between $y/d = 2.2$ and 3.4. The RSTM prediction for the lateral extent is also more accurate than that of the K–ϵ model. The RSTM placed the range of the lateral extent between $z/d = -1.54$ and 1.54, whereas the range predicted by the K–ϵ model is between $z/d = -0.74$ and 0.74. The experimental data showed the range of the lateral extent of the plume is actually between $z/d = -1.99$ and 2.0. Thus, the range predicted by the RSTM is 22% smaller than the experimental range, whereas the range predicted by the K–ϵ is 63% smaller than the experimental range.

Based on the information just presented, several general observations about the accuracy of the turbulence models are appropriate. The choice of turbulence model does not have a significant effect on the predicted value of the U component of velocity outside of the boundary layer. To within 7%, both turbulence models correctly predict the value of U at station 20. In contrast, model selection has a significant effect on the distribution and magnitude of τ_{xy}. Generally, correct predictions of the shape and magnitude of τ_{xy} contours by the RSTM demonstrate the validity of this model for TJISF. The incorrect prediction of the distribution of τ_{xy} with the K–ϵ formulation indicates that this model is not appropriate for accurate simulation of TJISF. Therefore, further simulation results from the K–ϵ model are not reported here.

Flowfield Analysis

An evaluation of the flowfield shock structure generated by the injection is presented in this section. Furthermore, a description of the mechanisms resulting in the secondary flowfields is presented. This analysis brings to light two significant facts associated with injection flowfields. First, the shock structure downstream of the oblique barrel (OB) shock is a mirrored reflection of the shock structure upstream of the OB shock, and second, the downstream vortical motion within the plume is a result of this mirrored shock structure and the upwash of inflow air deflected from the test-section surface behind the nozzle orifice.

The pressure ratio used by McCann and Bowersox[5] for the injectant and inflow air was insufficient to form a Mach disk at the top of the expansion plume or a sonic barrel shock around the plume. This situation is reflected in Fig. 7, which is a contour plot of the Mach number at the test-section centerline. However, Fig. 7 shows that a shock disk and an OB shock do form as a result of pressure equalization. The barrel shock is called oblique because outside of the boundary layer it does not cause a sonic condition around the plume.

The expanding injection plume has characteristics similar to an underexpanded rocket exhaust.[30] Like a rocket exhaust, the injectant plume contains alternating regions dominated by expansion and compression waves reflecting off of the plume boundaries. However, unlike the rocket exhaust, the inflow air impacting on the upstream side of the injectant plume results in a nonuniform backpressure acting on the injectant plume. This backpressure nonuniformity and the bending of the plume boundary result in a highly three-dimensional shock/expansion pattern within the plume.

As seen in Fig. 7, the volume defined by the OB shock can be divided into four separate regions. These regions are defined by the OB shock boundaries and the reflection lines shown in Fig. 7. The edges of the OB shock are the points where the expansion waves are reflected back into the plume as compression waves. At the point where the compression waves cross and converge, a shock forms.[33] In this flowfield the result is the shock disk at the top of the plume. The y–z reflection line roughly represents the vertical location in this plane, where the expansion waves are reflected off the plume boundary as compression waves. Subsequent figures will show that the impact the OB shock has on the downstream shock structure is delineated by this line.

By examining two-dimensional slices of the jet plume in each of the three coordinate planes, Chenault[30] has shown that region I of the plume is primarily composed of expanding injectant with a small degree of reflected compression waves. Region II is composed of a mixture of expanding injectant from the nozzle and reflected compression waves from the upstream regions of the plume, and region III is a mixture of reflected compression waves from the lower regions of the plume that are then reflected downstream as expansion waves. Finally, region IV is composed almost entirely of compression waves converging from the other three regions of the plume.

Several important surface structures of the flowfield and their approximate locations are illustrated in the numerical oil smear shown in Fig. 8. This representation is generated with streamtraces of the U and W velocity components for the computational cells adjacent to the test-section surface. It must be noted that these streamtraces are only two-dimensional representations of the particle paths and the apparent continuity of the path for a single particle in this plane is an illusion created by the absence of the V component of velocity. Thus, at any point in the flowfield, fluid from a plane above this one may be replacing a fluid particle from this plane, which has moved to a higher elevation in the flowfield.

At the edges of the nozzle exit, the high-pressure injectant expands outward in all directions. This expansion causes boundary-layer separation upstream of the nozzle resulting in a recirculation zone of injectant between the nozzle and the upstream extrema of the boundary-layer separation line at $x/d = -1.48$. The experimentally measured extrema of the boundary-layer separation line is at $x/d = -1.55$; thus, there is only a $0.07d$ difference in the numerical and experimental data. Within this recirculating region the fluid is almost exclusively injectant. At the leading edge of the recirculation zone, the inflow deflects the injectant up from the test-section

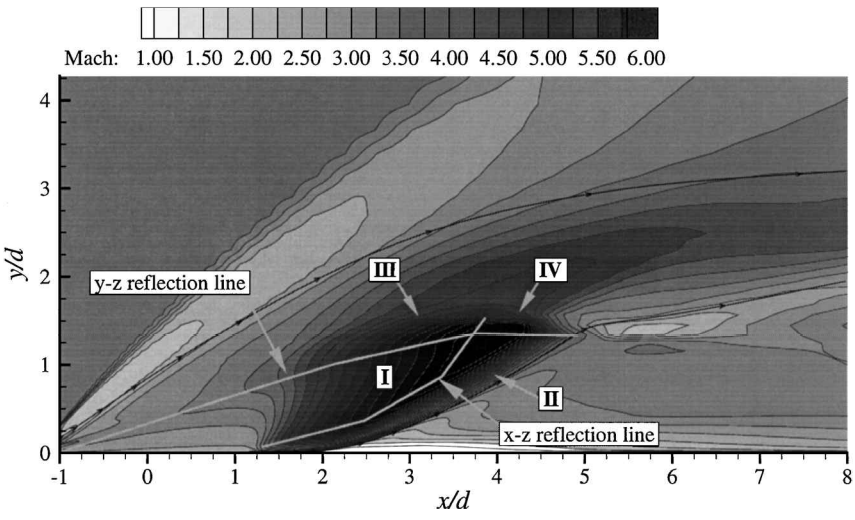

Fig. 7 Expansion and shock structure in the x–y plane.

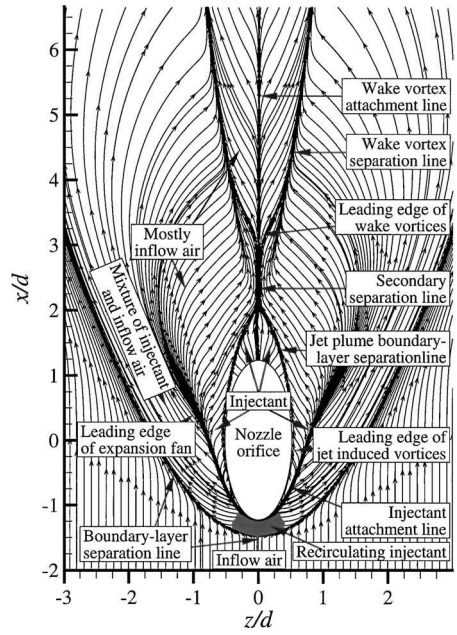

Fig. 8 Near-field numerical oil smear.

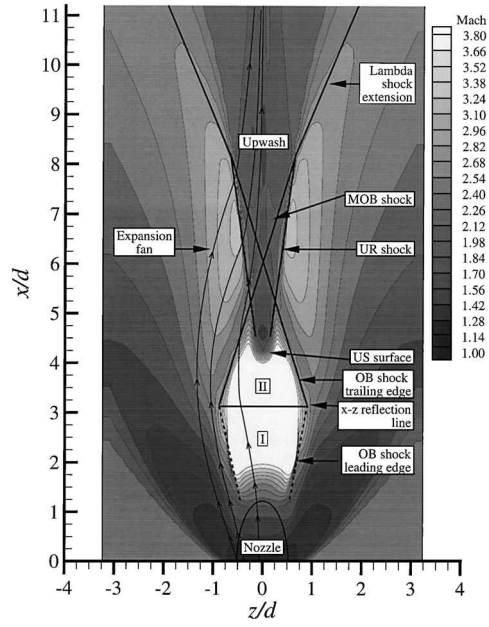

Fig. 9 Expansion and shock structure in x–z plane ($y/d = 0.91$).

surface and back downstream. This results in a horseshoe vortex forming behind the line, which defines the boundary-layer separation points. On the downstream side of this line, there is a thin layer of fluid containing injectant and inflow air. This layer is less than $0.01d$ thick, and the fluid above this layer is almost exclusively inflow air. However, because of the injectant's downstream deflection, it is possible for injectant to exist anywhere in the flowfield behind this line.

The outward expansion of the injectant leaving the nozzle between $x/d = -1.23$ and 0.0 is held in check by the inflow air that has moved up and over the horseshoe vortices. When the inflow air and the expanding injectant near the surface collide, part of the injectant is forced down to the surface and turned back in toward the nozzle. The impact points of the injectant with the test-section surface are on the attachment line seen in Fig. 8. The jet-induced (JI) vortices, which first appear near $x/d = -0.25$, are a result of the injectant turning back in toward the nozzle. Consequently, the fluid in the region between the attachment line and the edge of the nozzle, back to about $x/d = 0.5$, is almost exclusively injectant.

The lines on either side of the nozzle between the JI vortices and the edges of the nozzle mark the points where the plume separates from the test-section surface. These two separation lines converge as the plume rises above the surface and near $x/d = 2.0$; the two lines merge into a single secondary separation line. In the area between the plume separation lines, the fluid is exclusively injectant. When the plume begins to rise above the test-section surface, near $x/d = 0.5$, inflow air is drawn down to the surface and turned back in toward the centerline to fill the void left by the plume. The turning of the inflow air causes an expansion fan to form and accelerate the air. As the plume begins to separate from the test-section surface, the JI vortices are carried up along with it, and near $x/d = 0.5$ they also leave the vicinity of the surface. Near the point where the two plume separation lines merge, the inflow air moving in from either side of the nozzle collides. The line marking the collision points is the secondary separation line. We will show later in the discussion that the colliding inflow air not only turns back out away from the centerline, but is pushed up into the bottom of the plume. This upwash causes an upwash recompression (UR) shock in the jet wake and an upwash slip (US) surface forms in the impact region between the upwash and the jet plume.

Not all of the upwash is deflected up into the plume. Some of it is directed back down to the test-section surface, which forms two wake vortices near $x/d = 3.0$. The lines trailing downstream of $x/d = 3.0$ and away from the centerline are wake vortex separation lines. This line defines the Mach angle (approximately 10 deg) of the UR shock at the test-section surface. Finally, in Fig. 8, a wake vortex attachment line is identified between the wake vortex separation lines.

The flowfield shock structure below the y–z reflection line shown in Fig. 7 is shown in Fig. 9. Figure 9 shows that the OB shock has the characteristic diamond shock pattern described by Hill and Peterson of an underexpanded rocket exhaust.[34] In Fig. 9, parts of the OB shock are further categorized as either leading-edge or trailing-edge OB shocks. Region I, which is bounded in this plane by the leading edge OB shocks and the x–z plane reflection line, is composed almost exclusively of expansion waves originating from the nozzle upstream of $x/d = 0.0$ and by compression waves reflected from the upstream boundary of the plume. Region II, which is bounded in this plane by the trailing edge OB shocks and the x–z reflection line, is composed of expansion waves originating from the nozzle downstream of $x/d = 0.0$ and by compression waves reflected from regions of the plume upstream of the x–z reflection line. The effects of the compression waves in region II are stronger than the effects in region I because region II is downstream of the reflection line. The other labeled objects in Fig. 9 will be discussed after the upper part of the OB shock in the x–z plane is discussed.

The shocks in the upper part of the OB shock (above the y–z reflection line) are highly curved and form a tear-drop shape. This shape is characteristic of free-falling fluids in an atmosphere,[33] and the pressure of the inflow air has a similar effect on the shape of the OB shock. The region bound by the leading-edge OB shocks and the x–z reflection line (region III) is composed of reflected compression waves from the lower part of the plume and to a smaller degree, of expansion waves from the upstream parts of the plume. Region IV is almost exclusively composed of reflected compression waves from the other three quadrants of the plume. Thus, the shocks bounding this region are the strongest shocks encountered by the injectant as it leaves the OB shock/shock disk structure.

Several additional shock structures critical to the downstream description of the flowfield form in the wake of the OB shock and are also introduced in Figs. 9 and 10. Where the trailing-edge OB shocks cross in Figs. 9 and 10, a type I interference shock pattern of the form identified by Edney[35] and described by Emanuel[36] is formed. As shown by the minimal turning of the particle stream paths crossing the shocks in Fig. 9, the mirrored oblique barrel (MOB) shocks that formed below the y–z reflection line are very weak shocks. These are weak shocks because they are mirrors of the weak compression waves in region II of the OB shock.

The UR shock and US surface formed by the upwash from the inflow air collision are also identified in Fig. 9. As seen by the significant turning of the particle stream paths, in this part of the flowfield the UR shocks are stronger than the MOB shocks. The inflow air

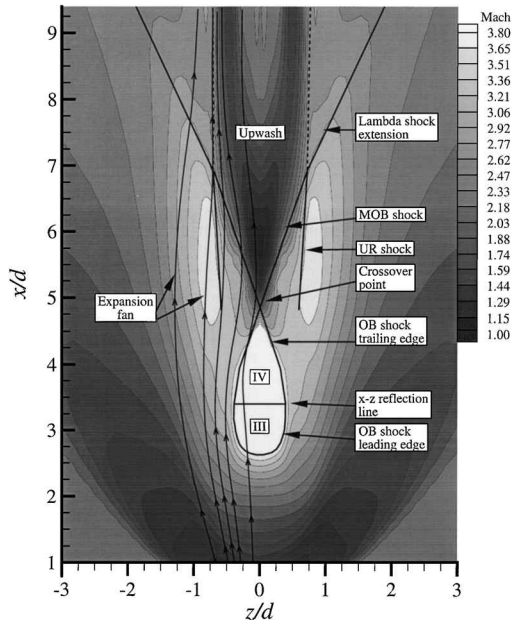

Fig. 10 Expansion and shock structure in x–z plane ($y/d = 1.45$).

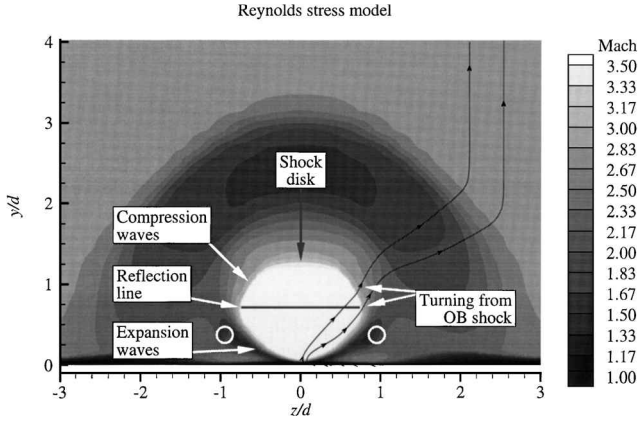

Fig. 11 Mach contours at $x/d = 2.00$.

expansion fan is seen outside of the various shock structures, and the nozzle orifice is also visible in Fig. 9.

Figure 10 shows that the relative strengths of the MOB shocks are significantly greater above the y–z plane reflection line than they are below it. Above this reflection line the MOB shocks are mirrors of the stronger compression waves identified in region IV of the OB shock structure. The combined effects of these shocks and the UR shocks result in a dramatic decrease in Mach number from Mach = 6.3 in the plume to Mach = 1.7 immediately downstream of the crossover point. Figure 10 also shows that the upstream edges of the UR shocks no longer intersect the OB shock in this plane. At the downstream intersection of these two shocks, a type VI interference shock pattern is formed, and in the expansion region of the interference pattern, the upwash forms a slip surface.

Complete separation of the injectant plume from the test surface occurs near $x/d = 2.00$, which is indicated in Fig. 11 by the rounding of the Mach contours on the underside of the plume. The contours on the underside of the plume are flat when the plume is attached to the surface.[30] At this station, in the y–z plane, the plume has assumed the classic shape of an underexpanded rocket exhaust. In Fig. 11 the formation of the expansion and compression waves is clearly evident. Again, below the y–z reflection line, the pressure equalization process is primarily expansion of the injectant; however, at the edges of the plume, the expansion waves reflect off of the boundary as compression waves and turn the path of the fluid particles thus forming the lower part of the OB shock. The turning caused by the compression waves is illustrated by the streamtrace that exits below

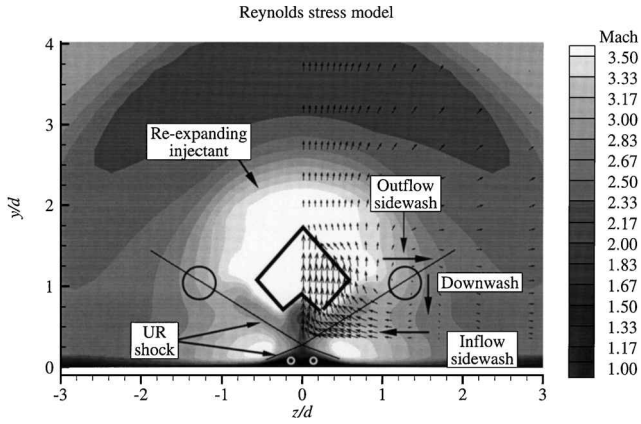

Fig. 12 Mach contours at $x/d = 4.00$.

the reflection line. Above the reflection line the compression waves converge to form the shock disk and the upper part of the OB shock. The turning caused by the upper part of the OB shock is illustrated by the streamtrace that exits above the reflection line.

Also annotated in Fig. 11 are the centers of rotation of the JI vortex pair. Note that the vortex centers of rotation have remained outside of the expanding part of the plume and below the y–z reflection line.

As indicated in Fig. 8, between $x/d = 2.0$ and 3.0, the sidewash of inflow air on either side of the test section collides at $z/d = 0.0$. In the wake of this collision, part of the air is deflected up into the bottom of the plume and creates an inflow upwash, and some of it is deflected down to the test-section floor creating the wake vortices. The impact between the upwash and the injectant on the lower side of the plume results in a US surface and a UR shock. This US surface is seen as the indentation at the bottom of plume, and the UR shock extends upward from the test-section surface crossing at a point above the wake vortices in the boundary layer.

As the flow continues to move downstream, more and more of the sidewash is turned up into the plume and down into the wake vortices. This causes a virtual compression ramp to form between $x/d = 3.0$ and 4.0. This virtual compression ramp acts as a guide that turns the sidewash up into the bottom of the plume.

A snapshot of the flowfield resulting from the events occurring between $x/d = 2.0$ and 4.0 is seen in Fig. 12. A diamond-shaped object outlining the edges of the OB shock is seen in this figure.

In addition to the flowfield features already discussed, the mechanism that sustains the rotation of the JI vortices is illustrated in Fig. 12. Shown in Fig. 12 is a complex mechanism of inflow air deflection and injectant leaving through the OB shock, which is sustaining the rotation of these vortices. From approximately $x/d = 0.5$ to the current location of $x/d = 4.0$, the rotation was sustained by the inflow sidewash originating in the expansion fan. This sidewash moves in toward the centerline and under the plume. When the inflow sidewash reaches the bottom of the plume, it is deflected up and out either by the injectant leaving the plume or it is turned by the OB shock. Thus, the opposing motion of the incoming sidewash and the outgoing sidewash of injectant and inflow air sustains the rotation started at $x/d = -0.25$.

Also, between $x/d = 2.0$ and 4.0, the JI vortices have moved still farther away from the test-section centerline and are beginning to move up and around the widest extent of the OB shock.

Between $x/d = 4.5$ and 5.0 the upwash completely passes through the terminus of the OB shock. Once this occurs, the upwash quickly moves deep into the plume and by $x/d = 5.0$ (Fig. 13) the US surface has moved to $y/d = 1.75$ from $y/d = 0.75$ at $x/d = 4.0$. Station 5.00 is also the downstream y–z plane where the trailing-edge OB shock and the MOB shock intersect. This crossover point is the convergence point of the two strong trailing-edge OB shocks from region IV. The crossover point is labeled in the Mach contours for this location (Fig. 13) and is seen as the sharp reduction in Mach number at the center of the plume.

As the flow moves downstream from $x/d = 5.0$ to 6.0, the MOB shock begins to spread, and a diamond-shaped pattern with an inverted tip at its bottom is seen in the Mach contours (Fig. 14). This

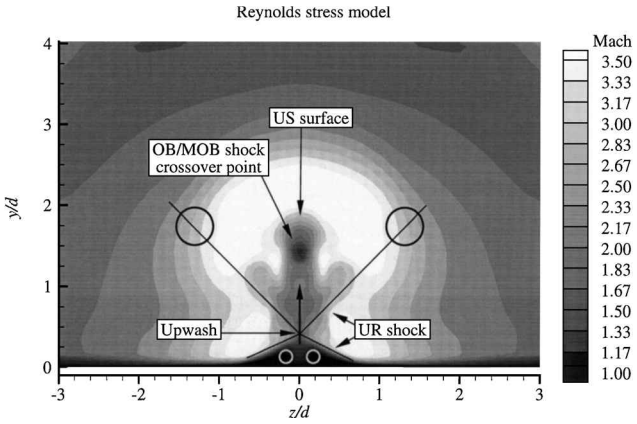

Fig. 13 Mach contours at $x/d = 5.00$.

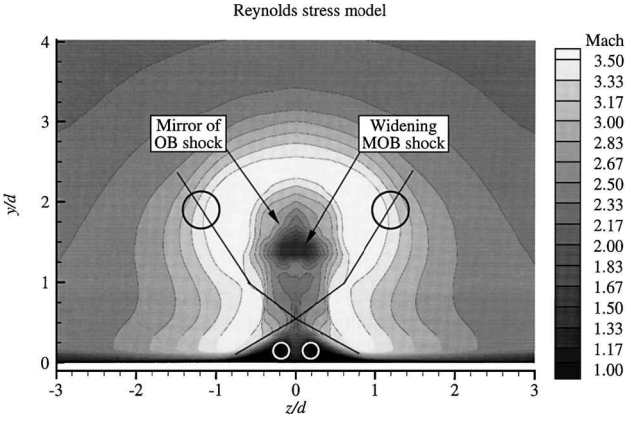

Fig. 14 Mach contours at $x/d = 6.00$.

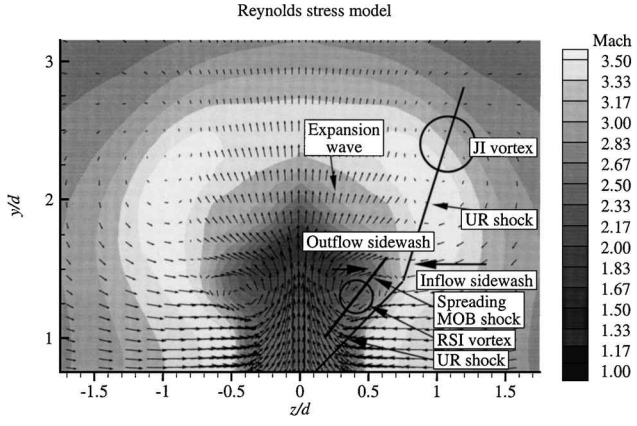

Fig. 15 Mach contours at $x/d = 7.00$.

diamond pattern is the extension trailing-edge OB shock mirrored across the crossover point near $x/d = 5.0$ (see Figs. 9 and 10). The outline of this diamond pattern is the same pattern visible upstream of the crossover point in Mach contours of Fig. 12 at $x/d = 4.0$. Figure 14 shows that the UR shock has developed a kink near the bottom of the plume. The cause of this kink becomes apparent in Fig. 15.

Between $x/d = 6.0$ and 7.0 a new vortex pair develops. The turning of the upwash, which generates these recompression shock-induced (RSI) vortices (Fig. 15), is caused by recompression as the upwash passes through the MOB shock and the subsequent re-expansion of the upwash as its pressure equalizes with the pressure of the surrounding fluid.

Figure 15 focuses on the activity near the center of the plume and shows the shock/expansion mechanism that generates the RSI

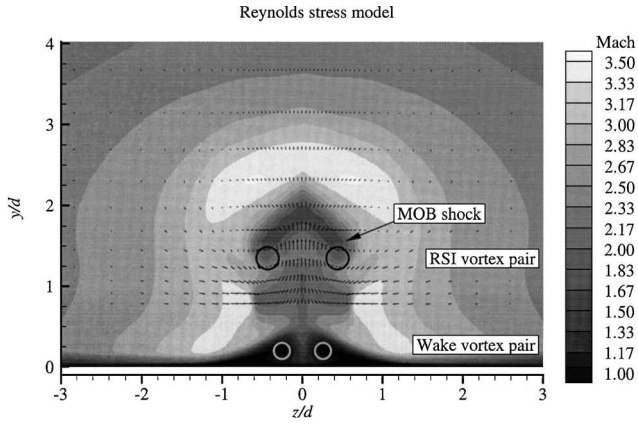

Fig. 16 Mach contours at $x/d = 8.00$.

vortices. This figure shows that the RSI vortices and the JI vortices are two separate phenomena, each having the same sense of rotation. Using the relative velocity vectors, the plume boundary can be defined as the point where the inflow and outflow sidewash vectors meet. Based on this definition, one can see that the RSI vortices are located within the plume and the JI vortices are outside of the plume. Hence, this is the first point within the injection flowfield where the traditional representation of the injection flowfield shown in Fig. 1 begins to form.

The mechanism that forms the RSI vortices is illustrated in Fig. 15. These vortices begin to form when the inflow sidewash passes through the UR shock and is turned upward and entrained with the already present upwash. The upwash then passes through the lower edge of the MOB shock. This further compresses the fluid and turns it upward along the test-section centerline. As a result of the compression, the upwash expands to equalize its pressure with the surrounding fluid. The expansion causes additional turning that results in a localized outflow sidewash. This outflow sidewash then encounters the upper edge of the MOB shock, where, once again, the flow is turned. However, this time it is turned down, creating a localized downwash. This downwash is then reflected off of the lower side of the plume boundary and back in toward the center of the test section. Thus, a rotation mechanism inside of the plume is established.

Outside of the plume, the mechanism sustaining the rotation of the JI vortices is disrupted by the expansion of the plume, and by the time the fluid reaches $x/d = 8.0$ (Fig. 16), the JI vortices have been engulfed by the expanding plume. With the consolidation of the RSI and JI vortices, the traditional representation of injection flowfield shown in Fig. 1 is established. Figures 9 and 10 show that the disruption of the mechanism sustaining the rotation of the JI vortices is coincident with intersection of the MOB and UR shocks between $x/d = 7.0$ and 8.0.

Prior to the consolidation of the RSI and JI vortices, lateral expansion of the plume is retarded by momentum and energy losses at the boundary between the plume and the surrounding fluid (for more details on this phenomenon, see Ref. 30). As seen in Fig. 15, at the plume boundary the outflow from the RSI vortices and the inflow from the JI vortices collide. This collision retards the lateral expansion of the plume. Figures 9, 10, and 16 show that once the RSI and JI vortices are consolidated the lateral expansion of the plume continues at an accelerated rate.

Run-Time Analysis

All of the computations for these simulations were performed on the Cray J916 computer located at the Aeronautical Systems Command Major Shared Resources Center, Wright–Patterson Air Force Base, Ohio. Typical run-time data for this simulation are presented in Table 3. These data show there is a linear increase in CPU time/grid point iteration, total run time, and memory requirements for each additional equation added to the governing equations. In other words, the RSTM simulation required five-sevenths more resources than that required for the K–ϵ simulation.

Table 3 Run-time analysis

Model	CPU time/grid point/iteration, μs	Total no. of iterations	Run time, $s \times 10^{-3}$	Memory required, MW
$K-\varepsilon$	19	8000	470	170
RSTM	32	8000	790	256

Conclusions

This study has presented a qualitative and quantitative comparison of the second-order ZSGS RSTM and ZSGS $K-\epsilon$ model to experimental data for a TJISF. This comparison showed the superiority of the RSTM to the $K-\epsilon$ model in predicting physically correct behavior of the turbulent crossflow shear stress. The RSTM prediction for the magnitude and distribution of τ_{xy} compared favorably with available experimental data. In contrast, the $K-\epsilon$ model had predicted magnitudes well but gave poor agreement with the distribution of the shear-stress data examined. The incorrect distribution of the shear-stress was brought about by the unidirectional evaluation of the velocity gradients imposed by the Boussinesq approximation.

An examination the flowfield predicted by the RSTM has provided greater understanding of the physical behavior of the flowfield immediately surrounding the nozzle orifice and the mixing mechanisms of an injection flowfield. The mechanism responsible for enhanced vortical motion of the flowfield was the MOB shock and the upwash created by collision of the inflow sidewash behind the injectant plume. Also, the interaction of these two flow phenomena resulted in the RSI vortices. These vortices formed downstream of the crossover point and inside the jet plume.

The desired lateral expansion of the plume was impeded by the JI vortices. The JI vortices, which were initially formed at the sides of the nozzle orifice, extended back along the sides of the jet plume, following the path of the UR shock as it propagated through the test section. The mechanisms that sustained the JI vortices retarded plume expansion by directing inflow sidewash back toward the center of the test section and into the plume. The mechanisms that generated the RSI vortices accelerated plume expansion by creating an outflow sidewash, forcing the injectant to move out away from the center of the test section. Once the MOB shock and the UR shock intersected with each other, the mechanisms sustaining the JI vortices were disrupted, and lateral expansion of the plume accelerated.

A major implication of the numerical results presented in the preceding section is that mixing enhancement can be accomplished if two elements of the flowfield are controlled: the location of the crossover point and amplification of the upwash deflected up into the plume.

The first element to enhanced mixing is moving the crossover point as close to the terminus of the OB shock as possible. This requires shaping the convergence angle of the trailing-edge OB shock in the $x-z$ plane. This angle should be as large as possible. A large angle will necessarily result in a shorter OB shock and an earlier crossover of the shocks. Control of these two factors may be possible by changing the shape of the nozzle orifice and the angle of injection. The elliptic nozzle and the 25-deg injection angle simulated in this study resulted in a convergence angle of approximately 20 deg and a crossover point about $5d$ downstream of the nozzle center. The shallow injection angle certainly contributed to the downstream elongation of the OB shock, and the elliptic shape of the nozzle may have contributed to the rather shallow convergence angle of the trailing-edge OB shocks. It seems reasonable that injection at a steeper angle with a circular nozzle will result in a crossover point closer to the nozzle exit. However, caution must be used in the selection of the injection angle because steeper injection angles will result in greater flow blockage and stronger bow shocks, both of which cause higher total pressure losses and, ultimately, thrust reduction.[9]

Upwash amplification is the second element suggested for mixing enhancement. We suggested here that the more fluid passing through the MOB shock, the more rotation will result. Wilson et al.[32] investigated a series of ramps and cones located immediately downstream of the injector port, and they found that the vorticity within the plume could be significantly enhanced or reduced depending on the ramp geometry. The expectation is based on the present analysis, that the influence of the ramp on the recompression shock was the primary mechanism responsible for the large changes in the downstream plume character. Further, the suggestion is made that proper shaping of downstream ramps using the method of characteristics to guide more of the upwash into the MOB shock will result in significant improvements in mixing efficiency and reduced total pressure losses.

Acknowledgments

Computational resources used for this study were sponsored by the U.S. Air Force Office of Scientific Research (AFOSR/NA) through Project/Task 2300/AS (Brian Sanders, Program Manager) and were provided by the Major Shared Resource Center at the Aeronautical System Center, Wright–Patterson Air Force Base, Ohio. The authors are grateful to Joseph Morrison, the developer of the program ISAAC. Morrison's many helpful hints and very extensive tutelage on the use of ISAAC were invaluable to the success of this study, and his assistance is enthusiastically acknowledged.

References

[1] Aso, S., Okuyama, S., Kawai, M., and Ando, Y., "Experimental Study on the Mixing Phenomena in Supersonic Flows with Slot Injection," AIAA Paper 91-0016, Jan. 1991.

[2] Aso, S., Okuyama, S., Ando, Y., and Fujimori, T., "Two-Dimensional and Three-Dimensional Mixing Flow Fields in Supersonic Flow Induced by Injected Secondary Flows Through Traverse Slot and Circular Nozzle," AIAA Paper 93-0489, Jan. 1993.

[3] Fuller, E., Thomas, R., and Schetz, J., "Effects of Yaw on Low Angle Injection Into a Supersonic Flow," AIAA Paper 91-0014, Jan. 1991.

[4] Mays, R., Thomas, R., and Schetz, J., "Low Angle Injection Into a Supersonic Flow," AIAA Paper 89-2461, July 1989.

[5] McCann, G., and Bowersox, R., "Experimental Investigation of Supersonic Gaseous Injection Into a Supersonic Freestream," *AIAA Journal*, Vol. 34, No. 2, 1996, pp. 317–323.

[6] Santiago, J., and Dutton, J., "Crossflow Vortices of a Jet Injected into a Supersonic Crossflow," *AIAA Journal*, Vol. 35, No. 5, 1997, pp. 915–917.

[7] Spaid, F., and Zukoski, E., "A Study of the Interaction of Gases Jets from Transverse Slots with Supersonic External Flows," *AIAA Journal*, Vol. 6, No. 2, 1968, pp. 205–212.

[8] Yokota, K., and Kaji, S., "Two and Three Dimensional Study on Supersonic Flow and Mixing Fields with Hydrogen Injection," AIAA Paper 95-6024, April 1995.

[9] Northam, G., and Anderson, G., "Supersonic Combustion Ramjet Research at Langley," AIAA Paper 86-0159, Jan. 1986.

[10] Mattingly, J., Heiser, W., and Daley, D., *Aircraft Engine Design*, AIAA Education Series, AIAA, New York, 1987, pp. 99–103.

[11] Rizzetta, D., "Numerical Simulation of Slot Injection Into a Turbulent Supersonic Stream," AIAA Paper 92-0827, Jan. 1992.

[12] McClure, T., and Ervin, E., "CFD Analysis of Circular Transverse Injector for a Scramjet Combustor," AIAA Paper 96-0729, Jan. 1996.

[13] Fuller, E. F., and Walters, R. W., "Navier–Stokes Calculations for 3D Gaseous Fuel Injection with Data Comparisons," AIAA Paper 91-5072, Dec. 1991.

[14] Hartfield, R., and Bayley, D., "Experimental Investigation of Angled Injection in a Compressible Flow," *Journal of Propulsion and Power*, Vol. 12, No. 2, 1996, pp. 442–445.

[15] Williams, S., and Hartfield, R., "An Analytical Investigation of Angled Injection into a Compressible Flow," AIAA Paper 96-3142, July 1996.

[16] Donohuem, J., Haj-Hariri, H., and McDaniel, J., "Vorticity Generation Mechanisms in Parallel Injection Schemes for Supersonic Mixing," AIAA Paper 92-3286, July 1992.

[17] Aso, S., Tannou, M., Maekawa, S., Okuyama, S., Ando, Y., Yamane, Y., and Fukuoa, M., "A Study on Mixing Phenomena in Three-Dimensional Supersonic Flow with Circular Injection," AIAA Paper 94-0707, Jan. 1994.

[18] Gerlinger, P., Algermissen, J., and Bruggemann, D., "Simulation of Turbulent Slot Injection of Different Gases into a Supersonic Air Stream," AIAA Paper 94-2247, June 1994.

[19] Rizzetta, D., "Numerical Investigation of Supersonic Wing-Tip Vortices," AIAA Paper 95-2282, June 1995.

[20] Speziale, C., "On Turbulent Secondary Flows in Pipes of Noncircular Cross-Section," *International Journal of Engineering Science*, Vol. 20, No. 7, 1982, pp. 863–872.

[21] Wilcox, D., *Turbulence Modeling for CFD*, DCW Industries, Inc., La Cañada, CA, 1993, pp. 213–235.

[22] Chenault, C. F., Beran, P. S., and Bowersox, R. D., "Second-Order Reynolds Stress Turbulence Modeling of Three-Dimensional Oblique Supersonic Injection," AIAA Paper 98-3425, July 1998.

[23]Zhang, H., So, R., Gatski, T., and Speziale, C., "A Near-Wall Second-Order Closure for Compressible Turbulent Flows," *Near-Wall Turbulent Flows*, edited by R. So, C. Speziale, and B. Launder, Elsevier, New York, 1993, pp. 209–218.

[24]Bowersox, R., "Turbulent Flow Structure Characterization of Angled Injection Into a Supersonic Crossflow," *Journal of Spacecraft and Rockets*, Vol. 34, No. 2, 1997, pp. 205–213.

[25]Morrison, J., "A Compressible Navier–Stokes Solver with Two-Equation and Reynolds Stress Turbulence Closure Models," NASA CR-4440, May 1992.

[26]Morrison, J., Gatski, T., Sommer, T., Zhang, H., and So, R., "Evaluation of a Near-Wall Turbulent Closure Model in Predicting Compressible Ramp Flows," *Near-Wall Turbulent Flows*, edited by R. So, C. Speziale, and B. Launder, Elsevier, New York, 1993, pp. 239–250.

[27]van Leer, B., "Toward the Ultimate Conservative Difference Schemes V. A Second Order Sequel to Godunov's Method," *Journal of Computational Physics*, Vol. 32, No. 1, 1979, pp. 101–136.

[28]Roe, P., "Approximate Riemann Solvers, Parameter Vectors, and Difference Schemes," *Journal of Computational Physics*, Vol. 43, No. 2, 1981, pp. 357–372.

[29]Venkatakrishnan, V., "Preconditioned Conjugate Gradient Methods for the Compressible Navier–Stokes Equations," *AIAA Journal*, Vol. 29, No. 7, 1991, pp. 1092–1100.

[30]Chenault, C. F., "Analysis of Turbulence Models as Applied to Two- and Three-Dimensional Injection Flows," Ph.D. Dissertation, Dept. of Aeronautics and Astronautics, U.S. Air Force Inst. of Technology, AFIT/DS/ENY/98M-01, Wright–Patterson AFB, OH, March 1998.

[31]Vandromme, D., and HaMinh, H., "About the Coupling of Turbulence Closure Models with Averaged Navier–Stokes Equations," *Journal of Computational Physics*, Vol. 65, No. 2, 1986, pp. 386–409.

[32]Wilson, M., Bowersox, R., and Glawe, D., "Role of Downstream Ramps on Penetration and Mixing for Supersonic Injection Flows," AIAA Paper 97-2887, July 1997.

[33]Shapiro, A., *The Dynamics and Thermodynamics of Compressible Fluid Flow*, Vol. 1, Wiley, New York, 1953, pp. 565–567.

[34]Hill, P., and Peterson, C., *Mechanics and Thermodynamics of Propulsion*, 2nd ed., Addison–Wesley, Reading, MA, 1992.

[35]Edney, B., "Effects of Shock Impingement on the Heat Transfer Around Blunt Bodies," *AIAA Journal*, Vol. 6, No. 1, 1968, pp. 15–21.

[36]Emanuel, G., *Gas Dynamics: Theory and Applications*, AIAA Education Series, AIAA, New York, 1986, pp. 201–205.

R. M. C. So
Associate Editor